

SPECIAL TOPIC • OPEN ACCESS

The role of turbulence–flow interactions in L- to H-mode transition dynamics: recent progress

To cite this article: L. Schmitz 2017 *Nucl. Fusion* **57** 025003

View the [article online](#) for updates and enhancements.

You may also like

- [Overview of L- to H-mode transition experiments at ASDEX Upgrade](#)
U Plank, R M McDermott, G Birkenmeier et al.
- [Dynamics of L–H transition and I-phase in EAST](#)
G.S. Xu, H.Q. Wang, M. Xu et al.
- [Study on the L–H transition power threshold with RF heating and lithium-wall coating on EAST](#)
L. Chen, G.S. Xu, A.H. Nielsen et al.

The role of turbulence–flow interactions in L- to H-mode transition dynamics: recent progress

L. Schmitz

Department of Physics, University of California Los Angeles, Los Angeles, CA 90095, USA

E-mail: lschmitz@ucla.edu

Received 27 May 2016, revised 3 October 2016

Accepted for publication 11 October 2016

Published 9 January 2017



Abstract

Recent experimental and simulation work has substantially advanced the understanding of L-mode plasma edge turbulence and plasma flows and their mutual interaction across the L–H transition. Flow acceleration and $\mathbf{E} \times \mathbf{B}$ shear flow amplification via the turbulent Reynolds stress have been directly observed in multiple devices, using multi-tip probe arrays, Doppler backscattering, beam emission spectroscopy, and gas puff imaging diagnostics. L–H transitions characterized by limit-cycle oscillations (LCO) allow probing of the trigger dynamics and the synergy of turbulence-driven and pressure-gradient-driven flows with high spatio-temporal resolution. L-mode turbulent structures exhibit characteristic changes in topology (tilting) and temporal and radial correlation preceding the L–H transition. Long-range toroidal flow correlations increase preceding edge-transport-barrier formation. The energy transfer from the turbulence spectrum to large-scale axisymmetric flows has been quantified in L-LCO and fast L–H transitions in several devices. After formation of a transient barrier, the increasing ion pressure gradient (via the $\mathbf{E} \times \mathbf{B}$ flow shear associated with diamagnetic flow) sustains fluctuation suppression and secures the transition to H-mode. Heuristic models of the L–H trigger dynamics have progressed from 0D predator–prey models to 1D extended models, including neoclassical ion flow-damping and pressure-gradient evolution. Initial results from 2D and 3D reduced fluid models have been obtained for high-collisionality regimes.

Keywords: L–H transition, turbulence, predator–prey model, Reynolds stress

(Some figures may appear in colour only in the online journal)

1. Introduction

High confinement-mode (H-mode [1, 2]) operation is almost certainly required in future burning plasma experiments to achieve economical fusion energy production. Access to H-mode requires sufficient auxiliary heating power, and is challenging in large fusion plasmas where neutral beams at very high energy would be required to heat the core plasma. The 2008 International Tokamak Physics Activity (ITPA) scaling law for the L–H transition power threshold $P_{\text{th}} (\text{MW}) = 0.049 B_{\phi}^{0.8} n_e^{0.72} S^{0.94}$ [3] is

derived from an international, multi-machine database. This scaling reflects only the dependence of the L–H transition power threshold on plasma density $n_e (10^{20} \text{ m}^{-3})$, toroidal magnetic field B_{ϕ} (T), and the plasma surface area S (m^2). However, the threshold power has been shown to depend on additional parameters such as isotopic plasma composition, plasma shape, divertor geometry, and the beam-induced and intrinsic torque [4–8]. A physics-based model of the L–H transition threshold power is therefore needed to confidently extrapolate to auxiliary heating requirements for ITER and future burning plasma experiments. It was recognized early on that the H-mode edge barrier forms as fluctuations are suppressed due to $\mathbf{E} \times \mathbf{B}$ flow shear [9–11] in a narrow (few cm wide) radial layer just inside the last closed flux surface (LCFS) [12–15]. While the paradigm of



Original content from this work may be used under the terms of the [Creative Commons Attribution 3.0 licence](#). Any further distribution of this work must maintain attribution to the author(s) and the title of the work, journal citation and DOI.

flow-shear suppression has been experimentally verified in the H-mode edge transport barrier as well as in internal transport barriers [16–18], the sequence of events leading to the formation of a highly sheared $E \times B$ jet flow layer has been the subject of intensive research. In particular, the causality of shear layer formation and pressure-gradient increase has been under investigation in many different toroidal confinement devices. Understanding the trigger event or mechanism initiating formation of a highly localized shear-flow layer, and understanding the spatio-temporal evolution of both the edge flow layer and the turbulence properties are important steps towards developing a physics-based L–H transition model. Within the last decade, significant progress has been made in mapping the evolution of turbulence and flows across the L–H transition. Significant improvements in edge diagnostics, including gas puff imaging (GPI), multi-channel Doppler backscattering (DBS), and high-resolution charge-exchange recombination spectroscopy, have substantially contributed to these advances.

In particular, the role of self-organized, turbulence-driven flows [19–23] as a trigger or prerequisite of the L–H transition has attracted considerable interest [24–26]. Periods of reduced turbulence and reversed poloidal turbulence flow and flow shear have been detected preceding the L–H transition in NSTX [28]. A large body of recent experimental work [27–39] strongly points towards turbulence-enhanced, sheared $E \times B$ flow as the critical element in triggering local fluctuation suppression preceding the L–H transition. Turbulence–flow interaction can enhance the mean ion flow (radial scale \sim minor radius a , or pressure-gradient radial scale length L_p) via amplification of pre-existing (L-mode) seed shear flow, mediated by the Reynolds stress [19, 24]. Turbulence–flow interaction can also manifest in the form of mesoscale zonal flows (ZFs) [40, 41], characterized by poloidally/toroidally symmetric $E \times B$ flows with a mesoscale radial structure ($\rho_i < \lambda_r < 2\pi/k_r^{ZF} < L_p$, where ρ_i is the ion Larmor radius, λ_r is the radial-turbulence correlation length, and k_r^{ZF} is the ZF radial wavenumber). In the literature, axisymmetric turbulence-driven mean ion flows and ZFs are not always clearly delineated in terms of spatial or temporal scale separation, and the terms are sometimes used interchangeably. The energy transfer from the turbulence spectrum into low-frequency turbulence-driven flows, via the nonlinear Reynolds stress, has been directly measured recently during edge barrier formation, supporting the physical picture of shear-flow amplification [35, 36, 38, 39, and others] leading to simultaneous turbulence quench. In this paper we review recent experimental evidence of turbulence–flow interaction in the edge of L-mode plasmas and across the L–H transition, as well as recent simulation work based on heuristic transitions models and reduced magnetohydrodynamics (MHD) and fluid models.

In addition to so-called ‘fast’ or ‘one-step’ L–H transitions, much recent research has focused on transitions characterized by an intermediate oscillatory phase between L- and H-mode (dubbed I-phase or LCO (limit-cycle oscillation) phase). The intermediate phase is characterized by a periodic increase in sheared $E \times B$ flow velocity, and concomitant reduction in

fluctuation levels, and has been observed in multiple devices (ASDEX and ASDEX-Upgrade (AUG) [29, 42–44], JET [45], TJ-II [28, 31, 46, 47], DIII-D [32, 36, 48–52], EAST [30, 53, 54], HL-2A [33, 55, 56], JFT-2M [57], and others). It is important to note that ‘I-phase’ is distinct from ‘I-mode’ which denotes an enhanced confinement regime with edge-temperature pedestals similar to H-mode, but without a density pedestal. LCOs are most often (but not exclusively) observed near the L–H transition power threshold, with the ion grad- B drift directed in the favorable direction (towards the active divertor) or in a double-null divertor configuration, and can be characterized as an intermediate state between L-mode and H-mode, where periodic increases in the radial electric field inside the LCFS, and concomitant periodic turbulence reduction or suppression occur. LCO transitions allow investigation of L–H transition physics with unprecedented temporal and spatial resolution.

0D and 1D heuristic dynamical models of the L–H transition [58–65] have advanced substantially during the last five years and now include radial particles, momentum, and energy transport. 1D models have recently also been used to investigate L–H power-threshold scaling [60, 65]. 2D and 3D fluid models [66–73], mostly in simplified slab or toroidal slab geometry, have been used to model the L–H transition sequence for high collisionality regimes, with equation systems appropriate for interchange or resistive ballooning turbulence.

The goal of this paper is to review recent work on turbulence–flow interactions in different toroidal devices, and to summarize the pertinent experimental findings. The paper is organized as follows: in section 2, the dynamics of transitions initiated via LCO is analyzed. Observed LCO properties on different devices are reviewed. Section 3 reviews measurements of long-range toroidal-flow correlations across transitions to enhanced confinement states, and stationary zonal flows. Section 4 discusses shear decorrelation and 2D eddy dynamics. Section 5 describes measurements of the Reynolds stress and the nonlinear energy transfer from turbulence to large-scale driven flows. Section 6 describes progress in modeling of L-mode-LCO and ‘fast’ L–H transitions.

2. L–H transitions initiated via LCO

So-called ‘dithering’ L–H transitions were observed early on the ASDEX [42, 43] and JET [45] tokamaks and, in ASDEX, interpreted as successive L–H and H–L transitions within a bifurcation model. In 2010, experiments at the TJ-II stellarator revealed periodic oscillations of the turbulence intensity and the edge electric field preceding the L to H-mode transition [28], with the radial electric field and $E \times B$ drift lagging the normalized density-fluctuation amplitude by $\pi/2$ (figures 1(a) and (b)). This result was suggestive of a predator–prey relationship between the turbulence intensity (prey) and the turbulence-amplified shear flow (the predator). An earlier 0D predator–prey model predicts this phase relationship [26], essentially incorporating a set of Lotka–Volterra equations for the turbulence driven flow (the predator) and the turbulence intensity (the prey), and an additional equation describing pressure-gradient evolution. As LCOs develop, the $E \times B$

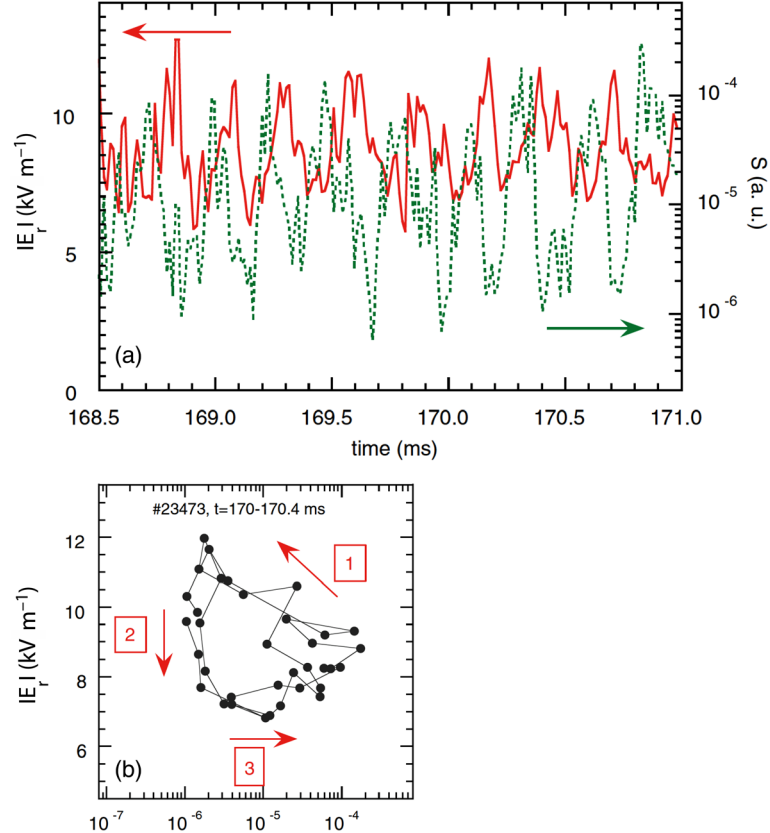


Figure 1. (a) Absolute value of the radial electric field and the turbulence intensity versus time showing LCO; (b) phase portrait of LCO: absolute value of radial electric field versus turbulence intensity. Figure reproduced with permission from [28]. Copyright 2010 Europhysics Letters Association.

shear flow increases periodically, suppressing turbulence and allowing the ion pressure gradient to increase gradually. The $E \times B$ flow shear associated with diamagnetic flow increases over time and eventually dominates the turbulence-generated flow shear as the edge barrier forms. The H-mode transport barrier is sustained once equilibrium $E \times B$ flow shear due to the increasing pressure gradient maintains a low turbulence level and prevents the limit cycle from re-occurring. Hence, this model provides a route to a sustained H-mode state.

Evidence of LCO (also referred to as ‘I-phase’) preceding the L–H transition has been found in a number of experiments [27–33, 36, 53, 57]. In most of these experiments, periodic or intermittent low-frequency shear flows ($<5\text{kHz}$) were investigated; however, ZFs at the geodesic acoustic mode (GAM) frequency have also been documented [29]. In most experiments, LCOs have been investigated in a single-null divertor configuration with the ion grad- B drift directed towards the x-point (the favorable direction with a lower L–H transition power threshold), or in double-null configuration. However, LCOs have also been observed in configurations where the grad- B drift is directed away from the active divertor (unfavorable direction with higher threshold power). Figures 2 and 3 show the time evolution of the density-fluctuation level and the $E \times B$ velocity across the plasma edge in DIII-D ([32], as measured via DBS [74, 75]), and in the EAST tokamak (measured via GPI [53]). For the DIII-D (L-mode) data in figure 2, the plasma is in a lower single-null divertor

configuration with the ion grad- B drift directed towards the x-point (favorable drift direction), with $\langle n_e \rangle \sim 2.5 \times 10^{19} \text{ m}^{-3}$, $B_\phi = 2 \text{ T}$, and $q_{95} = 4$. The plasma current is $I_p = 1.1 \text{ MA}$. The injected neutral-beam power was raised from 0.85 MW to 4.2 MW about 25 ms before the L-LCO transition occurred.

Figure 2(a) shows the divertor D_α signal and a time evolution contour plot of the $E \times B$ velocity and normalized density-fluctuation level across and inside the LCFS, for DIII-D discharge #140426. The auxiliary heating (NBI) power level is, in this case, substantially above the L–H transition power threshold before the L-mode-LCO transition. The periodic decrease in the recycling light indicates modulation of the radial particle outflow past the LCFS due to periodically improved local radial particle confinement. LCOs are present before the final transition to H-mode occurs. The density-fluctuation level (figure 2(b)) and the $E \times B$ velocity (figure 2(c)) are determined via multi-channel DBS from the backscattered signal intensity and the perpendicular turbulence propagation velocity measured in the laboratory frame [74, 75]. This velocity is typically dominated by the $E \times B$ velocity, and the (plasma-frame) turbulence-phase velocity is typically small. Twelve radii are probed simultaneously by the DBS system. The DBS probing locations (x-mode cut-off layer) were determined for this data set via GENRAY ray tracing [76], based on high-time-resolution (25 μs) electron-density profiles from profile reflectometry [77]. Around 1288 ms, the transition to ELM-free (edge-localized mode-free) H-mode takes place

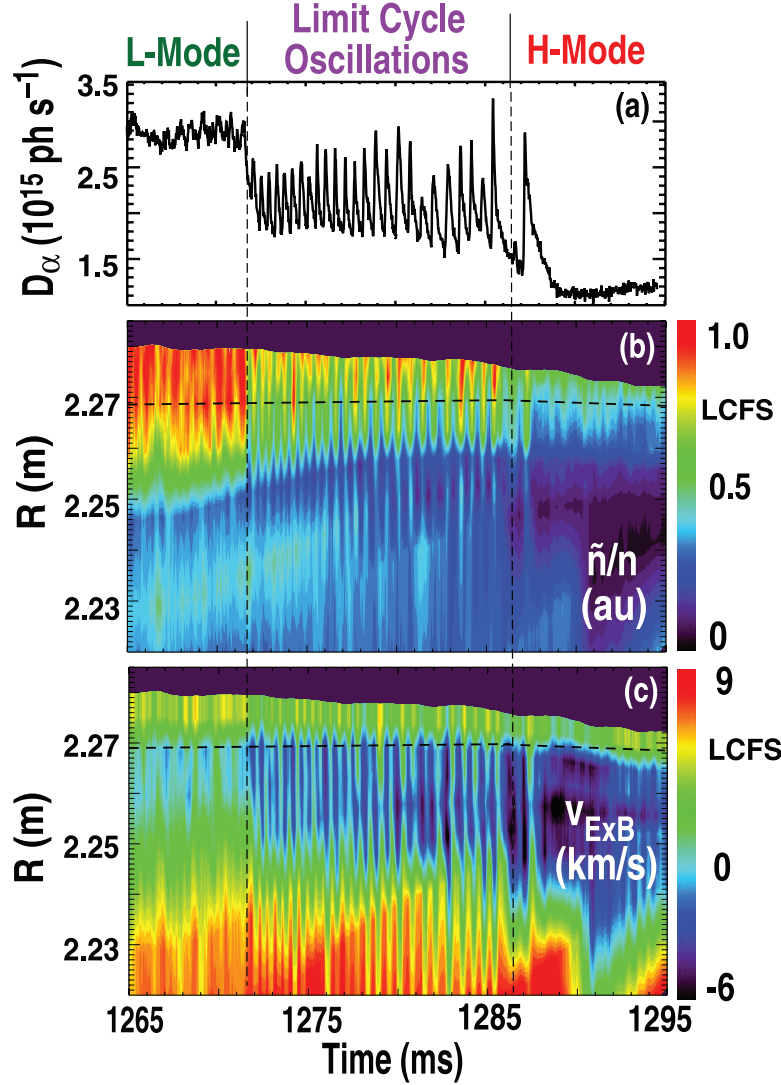


Figure 2. (a) Divertor D_α recycling light; (b) contour plot of normalized density-fluctuation level \tilde{n}/n versus time and major radius, across the L-mode-LCO–H-mode transition; (c) contour plot of $E \times B$ velocity versus time/major radius. Figure reprinted with permission from [32]. Copyright 2012 by the American Physical Society.

after a final transient, characterized by a radially extended steady flow layer. The normalized density-fluctuation level \tilde{n}/n (proportional to the amplitude of the scattered DBS signal) is highest at/outside the separatrix in L-mode and is periodically reduced during the LCO. Sustained turbulence reduction is observed at the LCO-H-mode transition at $t_H \sim 1288 \text{ ms}$ (Figure 2(b)). The probed poloidal wavenumber is $k_\theta \rho_s \sim 0.45$ with $\Delta k_\theta/k_\theta \sim 0.3$, consistent with the wavenumber range characteristic of the ion temperature gradient driven modes (ITG), trapped electron modes (TEM), and/or resistive ballooning modes (RBM). When the LCO starts at 1271.7 ms , the $E \times B$ velocity periodically becomes more negative at and just inside the LCFS. The negative flow increases with time and the flow layer expands radially inwards (figure 2(c)).

Figure 3 shows corresponding data (the D_α signal, density-fluctuation level, and poloidal turbulence advection velocity) during a transition from L-mode into an LCO phase (I-phase) and further into H-mode on the EAST tokamak [53]. L-mode plasma parameters for the EAST shot are similar to the DIII-D shot shown in figure 2, with $\langle n \rangle = 2.8 \times 10^{19} \text{ m}^{-3}$, $B_\phi = 1.78 \text{ T}$, $I_p = 0.4 \text{ MA}$, $q_{95} \sim 4.4$; however, in a double-null

divertor configuration. Lower-hybrid current-drive power of 1.2 MW and ion-cyclotron-resonance heating power of 1 MW was applied, with the (constant) effective power $P_{RF} \sim 1 \text{ MW}$ coupled to the plasma. Similar to the DIII-D data, oscillations are observed in the I-phase in the divertor D_α signal (figure 3(a)), the normalized density-fluctuation level (figure 3(c)), and in the poloidal turbulence advection velocity v_p (figures 3(d) and (e)), pointing in the electron diamagnetic direction inside the LCFS, and in the ion diamagnetic (positive) direction in the SOL. Shown is also the radial turbulence advection velocity (figure 3(f)) and the Reynolds stress $Re = \langle \tilde{v}_r \tilde{v}_\theta \rangle$ calculated via velocimetry from GPI data (figure 3(g)). A brief $\sim 100 \mu\text{s}$ time delay is observed between the periodically increasing density-fluctuation level (figure 3(b)) and the divertor D_α signal (indicated by dashed lines). This delay is due to the parallel-flow propagation time between the GPI imaging location above the tokamak midplane and the divertor. Flow and turbulence data cannot be reliably extracted during H-mode due to the low fluctuation level. The Reynolds stress (figure 3(g)) peaks when the turbulence level recovers periodically during I-phase, in turn increasing the poloidal turbulence advection velocity and

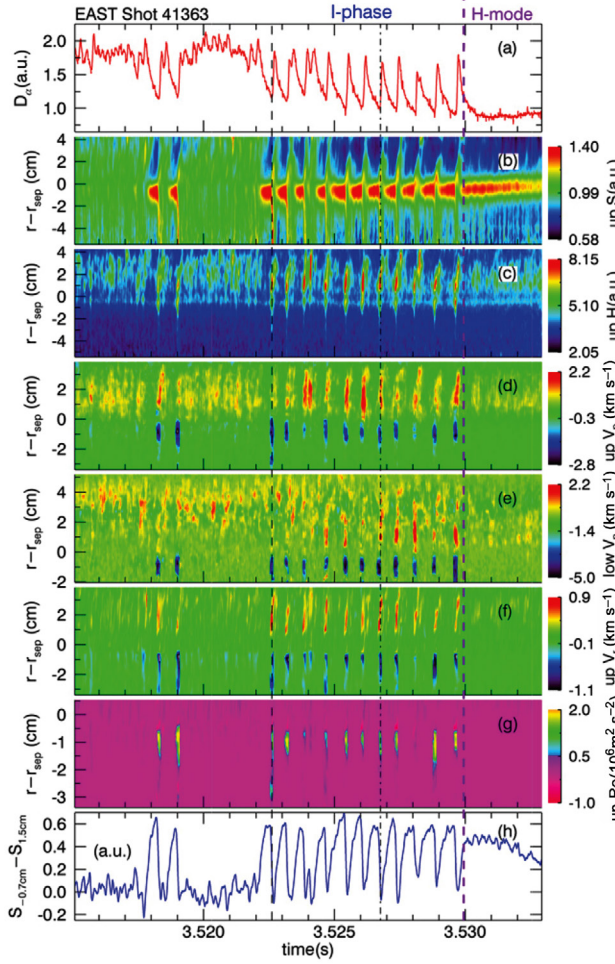


Figure 3. Time evolution of key parameters across an L-mode–I-phase–H-mode transition in EAST: (a) divertor D_α emission across a dithering (LCO) L–H transition; (b) contour plot of measured GPI-emission intensity; (c) turbulence level derived from GPI; (d)–(e) poloidal turbulence advection velocity from two poloidally separated GPI systems/views; (f) radial turbulence advection velocity calculated from GPI data; (g) Reynolds stress $Re = \langle \tilde{v}_r \tilde{v}_\theta \rangle$ derived using data from the upper GPI system; (h) difference in GPI emission intensity between two radial locations 0.7 cm inside the LCFS and 1.5 cm outside the LCFS. Figure reproduced with permission from [53]. Copyright 2014 IAEA, Vienna.

flow shear and suppressing the turbulence. Figure 3(h) shows the differential of the GPI intensity inside and outside the LCFS, demonstrating that the plasma density inside the LCFS (and the radial density gradient across the LCFS) increases during the quiet periods until the turbulence re-emerges and the radial transport produces a burst of radial flux that is eventually reflected by the peak in divertor D_α emission. The magnitude of the periodic Reynolds stress enhancement appears to be consistent with the observed increase in poloidal advection, as discussed in more detail in section 5.

Depending on the specific experimental conditions, limit cycles (between the $E \times B$ velocity or shear, and the turbulence/density-fluctuation level) have been observed with clockwise or counterclockwise phase rotation. An increase in the shear following the peaking of the turbulence intensity is consistent with the 0D predator–prey dynamics. The opposite phase rotation is expected once the $E \times B$ shear is

mainly controlled by the ion pressure gradient through the ion diamagnetic velocity: A periodically increasing ion pressure gradient, as has been observed in several experiments once the LCO is well developed [30, 32, 33, 51–53], increases the local turbulence level beyond a critical-gradient threshold. The increasing turbulent transport then in turn flattens the pressure gradient and drives flow. The turbulence drive and fluctuation level are subsequently reduced, allowing the pressure gradient to steepen again. In HL-2A, a switch from clockwise to counterclockwise limit cycles has been observed in LCO that eventually transitioned to H-mode [33, 55, 56]. However the rotation direction of the limit cycle can also depend on radius if 1D effects are taken into account, for example due to radial propagation of turbulence-driven flows (changing the phase between $v_{E \times B}$ and \tilde{n}/n), or due to the radial dependence of the turbulence drive. In 1D, the limit-cycle direction does not by itself indicate causality of shear flow generation. Direct evidence for 1D effects is shown for example in [31, 32, 51]. The typical signature is a radial propagation of the $E \times B$ flow. In DIII-D, the flow propagates radially inward inside the LCFS, and outwards outside the LCFS. The radial inward propagation changes the phase shift between density-fluctuation level and $E \times B$ drift, and is consistent with a reversal of the limit-cycle direction near or inside the bottom of the E_r well. Outward propagation in the scrape-off layer (SOL) was recently also revealed in AUG [44]. It is not known at this time whether this radial dependence is universal in tokamaks. With different magnetic field topology in the TJ-II stellarator, for example, an outward propagation of the flow pattern has been observed inside the closed flux-surface region [31]. In a heuristic 1D predator–prey model simulating LCO, including zonal flow and mean flow evolution, as well as radial particle and heat transport, inward propagation of the mean flow oscillations inside the LCFS has also been observed [58]. The radial propagation delay, and the phase shift between the turbulence bursts and the peaks in the mean flow increase in this model as LCOs evolve. In DIII-D, the phase shift between the turbulence level (intensity) maxima and the flow maxima has been observed to increase as LCOs evolve. This phase shift reaches $\sim 180^\circ$ close to the LCO-H-mode transition [32].

In virtually all experiments the $E \times B$ shear associated with the ion diamagnetic flow eventually becomes dominant as the LCO/I-phase evolves. The increasing edge pressure gradient is, therefore, decisive for the LCO-H-mode transition, to lock in and maintain H-mode confinement [32, 38, 51–53]. The LCO cycle period increases in time towards the LCO-H-mode transition. Experimental evidence indicates that the increasing $E \times B$ shear due to the pressure gradient built up maintains fluctuation suppression for a longer time period in each successive LCO cycle before turbulence growth resumes and the turbulence-driven flow recovers. The LCO cycle frequency, therefore, decreases in time. A simple condition for the LCO-H-mode transition [78] can be derived from the flow equation described in [26, 58]: LCO will cease if the time derivative of the turbulence-driven flow becomes zero. This condition depends on the Reynolds stress, the flow-damping rate, and the pressure-gradient scale length. A rigorous analysis of the predator–prey system described in [26] can be

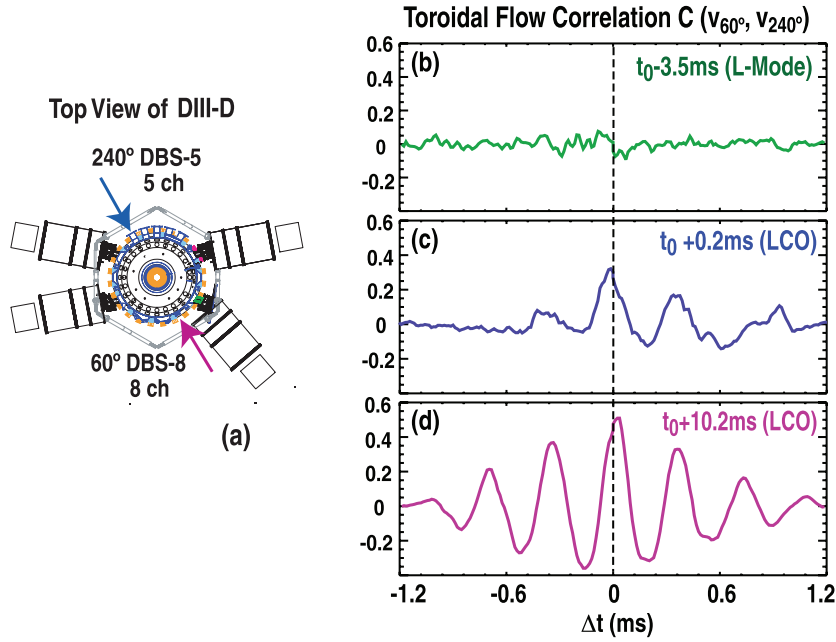


Figure 4. (a) Sketch of DIII-D tokamak indicating locations of toroidally spaced DBS systems; (b) toroidal-correlation coefficient of $E \times B$ flow during L-mode; (c) toroidal correlation across the L-mode-LCO transition; (d) toroidal correlation coefficient during fully developed LCO. Figure panels reproduced with permission from [32]. Copyright 2012 by the American Physical Society.

found in the literature [65, 78] but is beyond the scope of this paper. However, a simple model for the energy exchange between turbulence and flows is discussed in section 5.

LCO can exhibit a magnetic signature (on Mirnov arrays [44, 48, 49, 54]). In DIII-D the magnetic signature is observed when the diamagnetic flow is modulated in the LCO. A magnetic ($m = 0$) signature is then expected due to the periodic edge barrier formation and steepening of the edge pressure-gradient modulating the plasma's internal inductance. It has been pointed out in several experiments that LCO close to the H-mode transition can resemble type III ELMs, with a characteristic magnetic precursor ($n = 0, m = 1$) [48, 49]. In AUG, precursor oscillations and an $m = 1$ magnetic perturbation propagating in the ion diamagnetic direction, corresponding to or very similar to a type III ELM signature, has also been recently detected during extended LCO periods [44].

3. Long-range correlations and zonal flows

An important property of zonal flows and/or turbulence-driven mean ion flows is their global nature and correlation within the flux surface due to poloidal and toroidal symmetry. ZFs are characterized by poloidal and toroidal mode numbers $m, n = 0$, or $k_\theta, k_r = 0$ [40, 41]. Establishing poloidal/toroidal symmetry experimentally is, therefore, an important identification criterion. Probe measurements in the TJ-II stellarator revealed increased long-range toroidal correlations in the floating potential when the plasma was biased via an electrode inserted past the LCFS [79]. In contrast, turbulent density fluctuations exhibited short toroidal correlation length that decreased even more (together with the fluctuation level) when biasing was applied.

In DIII-D, toroidal/poloidal symmetry of the observed $E \times B$ velocity oscillation during LCO has been explicitly confirmed [32] by cross-correlating the instantaneous Doppler shift between two DBS channels launching the same frequency ($f = 67.5$ GHz) at different toroidal locations ($\phi_1 = 60^\circ$ and $\phi_2 = 240^\circ$) on the machine midplane (figure 4(a)). Hence, the same density/flux surface is probed at two locations separated by 180° toroidally. Figure 4(b) shows that there is no toroidal flow correlation in L-mode; however, the correlation coefficient increases substantially at the start of the oscillatory phase ($t = t_0 + 0.2$ ms) (figure 4(c)) and reaches $C \sim 0.6$ once the LCO is fully developed, consistent with the formation of a macroscopic low-frequency flow with $m = 0, n = 0$, at a frequency of ~ 1.7 kHz. Figure 4(d) shows that the correlation coefficient $C(v_{240}v_{60})$ peaks around zero time lag, confirming the axisymmetric nature ($k_\phi = 0, k_\theta = 0$) of the oscillating flow feature. Similar to the observations in TJ-II, no toroidal correlation was found for the density fluctuation spectrum, characterized here typically by $0.2 \leq k_\theta \rho_s \leq 2$ (or higher wavenumbers if electron temperature gradient turbulence is present). Density fluctuations have finite parallel wavenumber k_{par} but short (few cm) poloidal correlation length.

The transition to a highly correlated ($n, m = 0$) flow state has also been investigated in detail in the TJ-K stellarator, using a Langmuir probe array covering the entire poloidal plasma circumference [80]. Plasma biasing via an electrode inserted into the closed flux-surface region has been employed to produce a strong positive electric field with radial shear within the LCFS. With a positive bias of 100 V, the poloidal correlation of the fluctuating floating potential increased substantially. Figure 5(a) shows a contour plot of the maximum floating potential correlation coefficient in the edge region demonstrating clearly that floating potential fluctuations

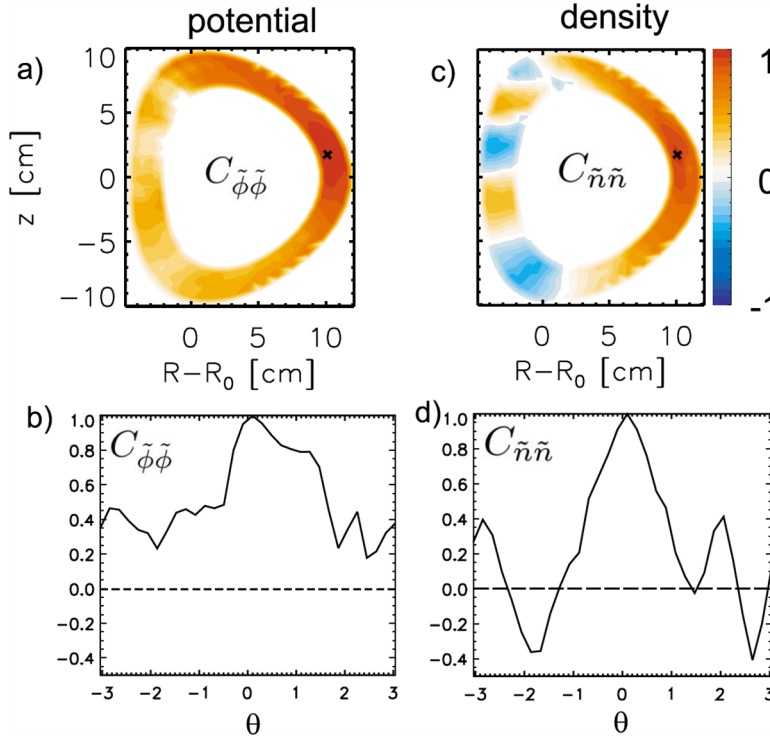


Figure 5. Poloidal correlation of density and potential fluctuation in the TJ-K stellarator with electrode biasing. (a) Contour plot of correlation coefficient of potential fluctuations (at zero time delay) as a function of poloidal angle and radius. Data from four different radii are included; the position of the reference probe is marked by a cross. (b) Correlation coefficient of potential fluctuations versus poloidal angle at the reference probe radius; (c) contour plot of density fluctuation correlation coefficient versus poloidal angle/radius; (d) density fluctuation correlation coefficient versus poloidal angle at reference probe radius. Figure taken from [80], with the permission of AIP Publishing.

(peaking in frequency below 10 kHz) are well correlated poloidally when positive bias is applied. In contrast, density fluctuations exhibit predominantly $m = 4$ and $m = 5$ poloidal structure and lower poloidal correlation (figure 5(c)). Figures 5(b) and (d) show the dependence of the correlation coefficient on poloidal angle at the biased electrode radius. Hence, in the presence of electrostatic biasing, these experimental results are consistent with the characteristics of zonal modes in the potential. A substantial decrease (by a factor of three) in broadband density and potential fluctuations is concomitantly observed with biasing. High-frequency (>30 kHz) density-fluctuation levels increase due to the Doppler shift resulting from increased poloidal flow; however, their contribution to the total fluctuation spectral power is small.

The experimental data in [79, 80] show clearly that potential fluctuations have much higher poloidal coherence with biasing, although the rms density-fluctuation level is somewhat reduced. It is perhaps surprising that flows driven from the turbulence spectrum via the Reynolds stress (see equation (1) below) could be maintained if the turbulence level decreases. However, the radial Reynolds stress gradient (and the seed flow shear localizing the turbulent structures) is likely modified by electrostatic biasing. Moreover the magnitude of the Reynolds stress does not only depend on the amplitude of radial and poloidal velocity fluctuations associated with drift-wave turbulence, but also on the coherence and relative phasing of these components.

Recent DBS results from the JET tokamak provide strong evidence of mesoscale zonal flows on the edge of ohmically

heated (OH) and L-mode plasmas [81]. JET exhibits a pronounced well structure in the radial electric field E_r already during the OH phase. The shear, in particular, in the inner shear layer increases substantially with NBI heating in L-mode, with a concomitant reduction of fluctuation levels. ZFs manifest as fine-scale radial structures (corrugations) within the radial electric-field well. Figure 6 shows the E_r profile and time-averaged density profiles during a 200 ms steady-state ohmic time window. With increasing plasma density, the radial wavelength of the ZFs decreases and their domain of existence moves outward. The mesoscale electric field structure varies with plasma conditions (density) at a fixed safety factor profile. Hence, it cannot be attributed to changes in the q -profile or to magnetic islands related to rational surfaces. Radial zonal flow shear is found to increase with collisionality. At low density, the fine-scale structure ZFs discussed here decrease in advance of the L–H transition and are not likely to be instrumental in the transition. However, at higher density, the ZF structure remains prominent throughout the L-mode phase and may provide, or contribute to, the shear flow that is instrumental in the L–H transition. In the higher density cases, fluctuation levels concomitantly exhibit an additional decrease in the center of the E_r well and in the inner shear layer across the L–H transition.

4. Shear decorrelation

The ratio of $\mathbf{E} \times \mathbf{B}$ shearing rate to the ambient turbulence decorrelation rate has been used to characterize the effects of $\mathbf{E} \times \mathbf{B}$ shear on turbulent eddy dynamics. According

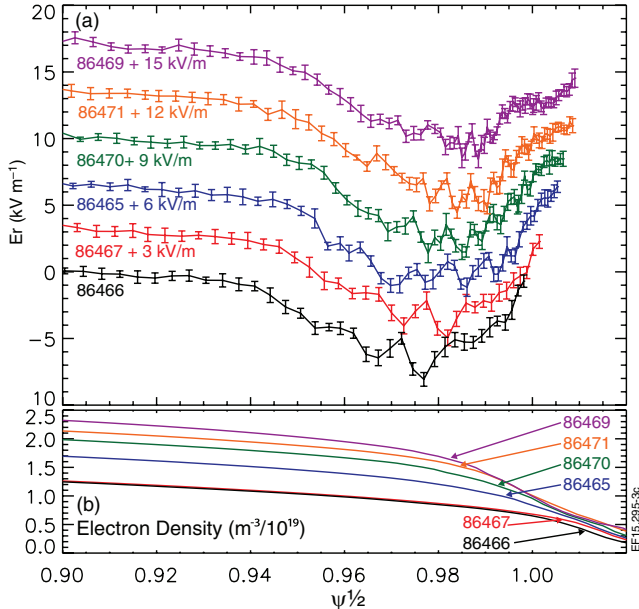


Figure 6. (a) Radial electric-field profiles in JET OH plasmas for six shots at different densities, $t = 12.4\text{--}12.6\text{s}$. For clarity, for each density increment the E_r profile is offset by an additional 3 kV m^{-1} (as annotated); (b) averaged plasma density profile $12.4\text{--}12.6\text{s}$, from a profile reflectometer. Figure reproduced with permission from [81]. Copyright 2016 by the American Physical Society, CC BY 3.0.

to the original theory by Biglari *et al* [9], shear decorrelation dominates ambient turbulence decorrelation for $\Delta\omega_D < (\Delta\omega_D \omega_{E \times B}^2)^{1/3}$ where $\Delta\omega_D$ is the ambient turbulence decorrelation rate and $\omega_{E \times B}$ is the $\mathbf{E} \times \mathbf{B}$ shearing rate. The turbulence-suppression criterion was found to be satisfied in tokamak plasmas just prior to the L-H transition and in H-mode [10, 11, 14], and also in internal transport barriers maintained via $\mathbf{E} \times \mathbf{B}$ shear primarily resulting from toroidal or poloidal ion rotation [16–18]. L-H transitions exhibiting LCO are particularly well suited to uncover the dynamics of shear-flow decorrelation due to the slow transition timescale. Figures 7 and 8 show the time history of two L-H transitions in AUG and DIII-D, illustrating the evolution of turbulence decorrelation and $\mathbf{E} \times \mathbf{B}$ shearing rate as the plasma enters an LCO. In AUG discharges near the L-H power threshold, the plasma transitions repeatedly between L-mode and I-phase, with a corresponding modulation in divertor current (indicative of the SOL outflow, figure 7(a)). Periodic oscillations in the perpendicular turbulence advection velocity [29] (used as a proxy for the $\mathbf{E} \times \mathbf{B}$ velocity) and the turbulence level (measured here for relatively high $k_\perp \sim 9.8\text{ cm}^{-1}$) are observed (figures 7(b)–(c)). During the ‘high flow’ state, GAM oscillations occur with a frequency of $\sim 15\text{ kHz}$, much higher than the limit-cycle frequency. Figure 7(d) shows a comparison of the equilibrium $\mathbf{E} \times \mathbf{B}$ shearing rate, the oscillating flow-shearing rate as an estimate of the GAM shearing rate, and the turbulence decorrelation rate, all extracted from DBS data. The turbulence decorrelation rate drops significantly at the onset of LCO, while the oscillating $\mathbf{E} \times \mathbf{B}$ flow-shearing rate increases and exceeds the decorrelation rate, satisfying the shear-suppression criterion. It is important to note that shearing rate and decorrelation rate remain similar once shear suppression takes

effect, as would be expected if flow shear governs turbulence decorrelation. The mean flow-shearing rate also increases when the plasma enters I-phase, but less significantly.

In DIII-D, the decorrelation and shearing rates have been determined across L-mode-LCO transitions characterized by low-frequency turbulence-driven flows (figure 8, [32]). The DBS diagnostic is applied, probing turbulence wavenumbers $k_\theta \sim 4\text{ cm}^{-1}$. Here, the turbulence-flow interaction manifests in localized poloidal ion flow within the LCFS, mediated by the perpendicular Reynolds stress, as described in more detail elsewhere [36, 39, 51, 52] and further below. GAM oscillations are observed in DIII-D L-mode plasmas routinely, but in contrast to the observations in AUG, decrease substantially in amplitude as the L-H or L-mode-LCO transition is approached [5]. Figure 8(b) shows clearly that the turbulence decorrelation rate decreases rapidly and matches the shearing rate preceding suppression of fluctuations, satisfying the shear suppression criterion. The shearing rate increases slowly and has a periodic modulation, exceeding the decorrelation rate during the time periods where turbulence is suppressed. Both the AUG and the DIII-D data indicate a substantial decrease in the decorrelation rate preceding turbulence suppression, which may be indicative of a topological change in turbulent eddy dynamics and/or spectral condensation into larger-scale structures with longer correlation times.

In a ‘fast’ L-H transition in the same lower single-null divertor configuration (#140439), but with beam power well above the transition threshold (L-mode density $\langle n \rangle \sim 1.5 \times 10^{19} \text{ m}^{-3}$), turbulence-driven, toroidally and poloidally axisymmetric $\mathbf{E} \times \mathbf{B}$ flows have been documented as short transients executing only part of one limit-cycle period over $\sim 2\text{ ms}$ [50]. Figure 9 shows the corresponding time evolution of density fluctuations (figures 9(a) and (c)), the total $\mathbf{E} \times \mathbf{B}$ shearing rate $\omega_{E \times B}$ and turbulence decorrelation rate $\Delta\omega_D$ (figures 9(b) and (d)), at two radii, and the radial density gradient (figure 9(e)). Just inside the LCFS the density-fluctuation level decreases as the flow-shearing rate exceeds the decorrelation rate (figures 9(a) and (b)). A brief flow oscillation corresponding to a partial LCO cycle is evident (figure 9(b)). Radial transport begins to decrease as reflected by the reduced D_α signal (figure 9(f)). Further inboard (about 2 cm inside the LCFS), the flow-shearing rate increases with a delay of 0.6–0.7 ms compared to the outboard location, again suppressing fluctuations once $\omega_{E \times B} > \Delta\omega_D$ (figures 9(c) and (d)). The radial density gradient increases mainly after fluctuations have been suppressed/reduced across the entire edge layer, and the further increase in $\omega_{E \times B}$ after 1294 ms can be ascribed to the increasing diamagnetic flow contribution, as the density (pressure) gradient steepens after the initial fluctuation suppression.

It is instructive to examine the dependence of density-fluctuation level and electric field for these data. Figure 9(g) shows two data sets for major radii 3.5–4.5 cm inside the LCFS. In contrast to transitions with multiple LCO cycles (figures 1–3), only one partial limit cycle is executed here during the transition. Hence, the ‘regular’ transition exhibits a similar phenomenology, on a condensed timescale, as the extended LCO transitions discussed earlier. Turbulence suppression due to flow shearing is first observed in both transition types near the separatrix when the turbulence decorrelation rate $\Delta\omega_D$

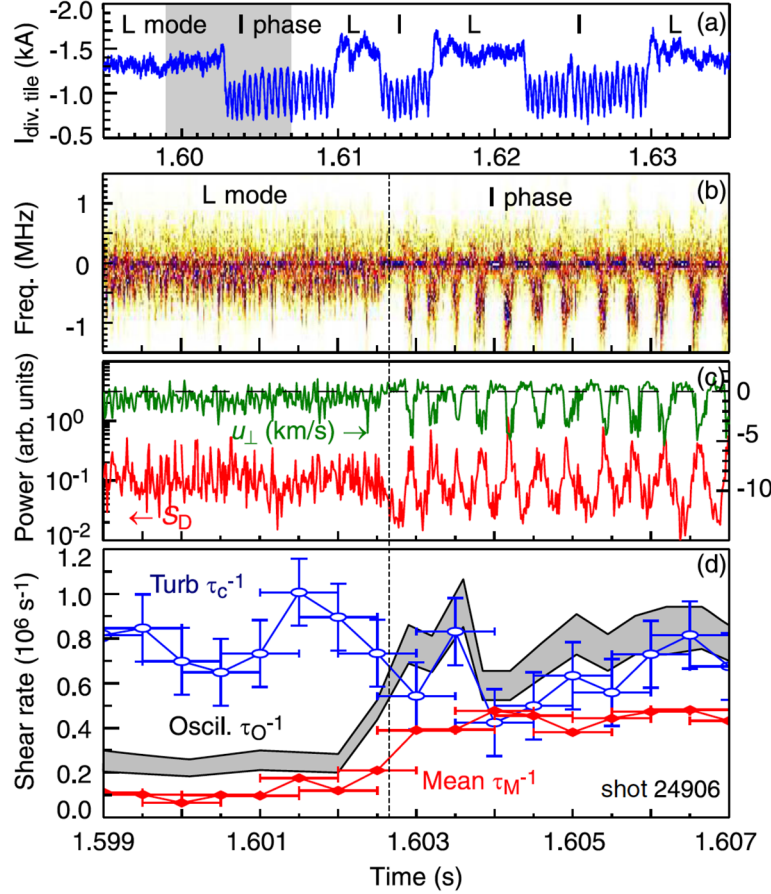


Figure 7. Time evolution of key parameters across the L-mode to I-phase transition in AUG: (a) divertor shunt current; (b) expanded Doppler reflectometer spectrogram $S(f)$ (darker shades correspond to higher turbulence intensity); (c) corresponding perpendicular advection velocity u_{\perp} and fluctuation level S_D from Doppler reflectometry, and (d) estimated mean and oscillatory shearing rates and turbulence decorrelation rate. Figure reproduced with permission from [29]. Copyright 2011 by the American Physical Society.

decreases sharply concomitantly with an increasing $E \times B$ shearing rate $\omega_{E \times B}$. The likely cause for this decrease in the decorrelation rate is a change in eddy topology concomitantly with the onset of turbulence (Reynolds-stress)-induced flow.

5. Turbulence–flow energy transfer and eddy dynamics

Turbulence–flow interactions can occur through ions’ mean flow acceleration or via zonal flows (ZFs [40, 41]) driven by the turbulence spectrum and, in turn, act back onto the turbulence spectrum via flow shearing/saturation. Turbulence–flow coupling is mediated via the perpendicular Reynolds stress. ZFs can manifest as zero-mean-frequency flows or GAMs [40, 41] with mesoscale radial extent ($\rho_s < 1/k_r^{\text{ZF}} < L_{p_i}$, where k_r^{ZF} is the typical ZF radial wavenumber and L_{p_i} is the radial pressure-gradient scale length). In either case the amplification of pre-existing (L-mode) shear flows via energy transfer from the turbulence spectrum is the crucial ingredient initiating the L–H transition sequence. A large body of experimental work has investigated turbulence–flow interaction in L–H transition dynamics [28–39]. Experimentally, it is often difficult to distinguish between mean flow and ZF shear flow amplification if only the turbulence advection velocity and the turbulence

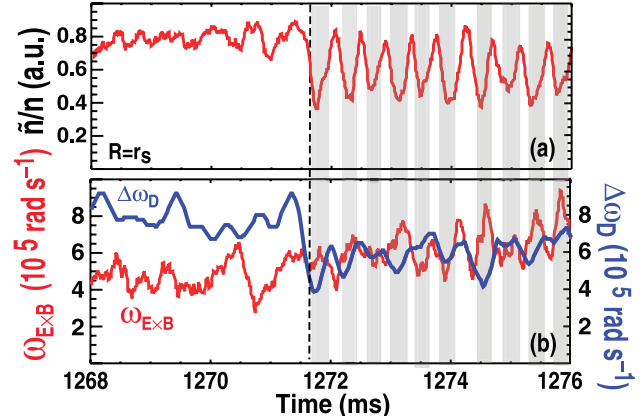


Figure 8. (a) Normalized density-fluctuation level from DBS data ($k_{\perp}\rho_s \sim 0.45$); (b) turbulence decorrelation rate $\Delta\omega_D$ and $E \times B$ shearing rate $\omega_{E \times B}$ across the L-mode-LCO transition (D-III-D data, figure panels reproduced with permission from [32]). Copyright 2012 by the American Physical Society).

rms amplitude can be measured. Gyrokinetic simulations for the core plasma [83–85] indicate that the zonal $E \times B$ flow is approximately balanced by diamagnetic flow (produced by pressure-profile corrugations), maintaining ion-momentum conservation (zero net poloidal flow of ions). However, near the separatrix and across the separatrix, poloidal ion

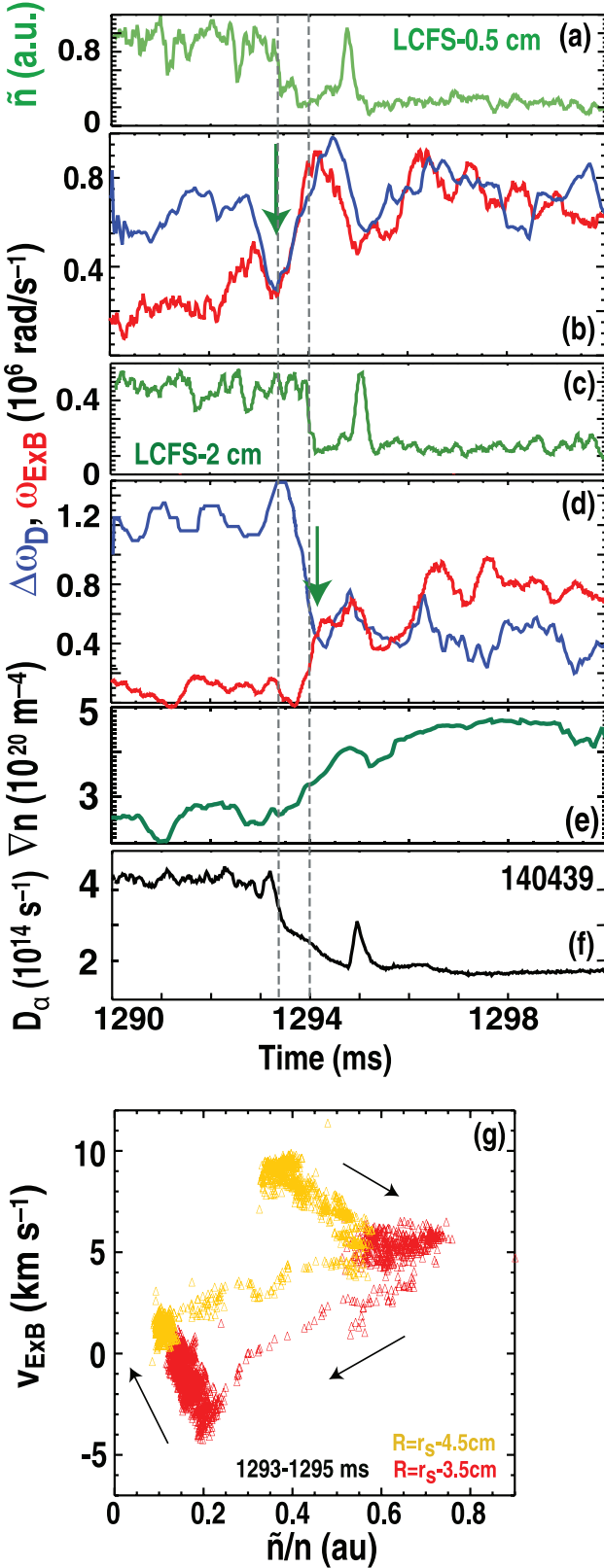


Figure 9. Time evolution of (a) normalized density-fluctuation level 0.5 cm inside the LCFS from DBS; (b) turbulence decorrelation rate and $E \times B$ shearing rate at the same radius; (c) normalized density-fluctuation level 2 cm inside the LCFS; (d) turbulence decorrelation rate and shearing rate 2 cm inside the LCFS; (e) plasma density gradient; (f) divertor D_α signal; (g) partial limit cycle across the L–H transition (DIII-D data, figure reproduced with permission from [50]. Copyright 2014 IAEA, Vienna).

momentum may not necessarily be conserved even on closed magnetic-flux surfaces due to ion orbits connecting closed and open field-line regions, and ZFs may not exhibit effective cancellation of $E \times B$ and diamagnetic flows.

Flow acceleration via the perpendicular Reynolds stress was proposed in 1990 as a mechanism for the generation of poloidal mean ion flow [19]. The change in poloidal velocity in the presence of a radial Reynolds stress gradient is described by equation (1):

$$(1 + 2q^2) \frac{\partial \langle v_\theta \rangle}{\partial t} = - \left\langle \frac{\partial}{\partial r} (\tilde{v}_r \tilde{v}_\theta) \right\rangle - \mu f(\langle v_\theta \rangle). \quad (1)$$

Here, $\langle v_\theta \rangle$ denotes the mean poloidal ion flow, $\langle \tilde{v}_r \tilde{v}_\theta \rangle$ is the perpendicular Reynolds stress, and μ is the poloidal flow-damping rate. The flow-damping term can be expressed as the flow-relaxation rate towards the neoclassical poloidal flow $\mu f(v_\theta) = \nu_\theta q^2 / \varepsilon^2 (\langle v_\theta \rangle - \langle v_\theta^{\text{neo}} \rangle)$, where ν_θ is the collisionality-dependent poloidal flow-damping rate, $v_\theta^{\text{neo}} = -K_1 \partial / \partial r (T_i / ZeB)$ is the neoclassical poloidal ion velocity with the collisionality-dependent constant K_1 [86, 87], and ε is the inverse aspect ratio. In the plateau regime, for example, $\nu_\theta = \nu_b \varepsilon^{1/2}$, where $\nu_b = v_i^{\text{th}} / qR$ is the ion-transit frequency. Poloidal flow inertia due to toroidal coupling has been taken into account here in the (left-hand side) acceleration term.

Finite Reynolds stress associated with flow generation requires that turbulent structures/eddies are elliptical in shape, and tilted in the poloidal direction. The direction of flow generation may largely depend on the geometry of the pre-existing L-mode shear flow (or seed shear flow). Seed shear flow can be associated with the diamagnetic flow due to the L-mode-edge pressure gradient and may reflect the neoclassical or intrinsic main ion flow. The eddy tilt direction will likely depend on the eddy location with respect to the radial profile of the seed shear flow. Taking advantage of advanced 2D GPI imaging capabilities, the topology, orientation and movement of blobs in the inside and outside the LCFS has been systematically studied in NSTX and Alcator C-Mod OH plasmas [88, 89]. A finite average Reynolds stress was found just inside and outside the LCFS in the NSTX data, with large standard deviations potentially consistent with oscillating zonal flows. Figure 10 shows a comparison of the poloidal flow velocity v_y and the Reynolds force acceleration $a_y = -\partial \langle \tilde{v}_r \tilde{v}_\theta \rangle / \partial r$ extracted from the GPI data taken in low-collisionality NSTX ohmically heated discharges (left panels). This data is compared with simulation results from the SOLT code: a 2D fluid code simulating the plasma edge within the LCFS and in the SOL, taking into account SOL sheath boundary conditions via appropriate closure relations (right panels). Both experimental and simulation data show acceleration in the negative (electron diamagnetic) direction and, concomitantly, a negative excursion in the flow velocity. As discussed in [88], the acceleration is more localized within the LCFS in the simulation and reverses sign in the SOL, in contrast to the experimental data showing a radially extended region of negative acceleration reaching into the SOL. The measured velocities ($\sim 1 \text{ km s}^{-1}$) and flow acceleration are naturally substantially smaller in the OH phase than across the L–H transition, as discussed in the following; however these measurements and simulations

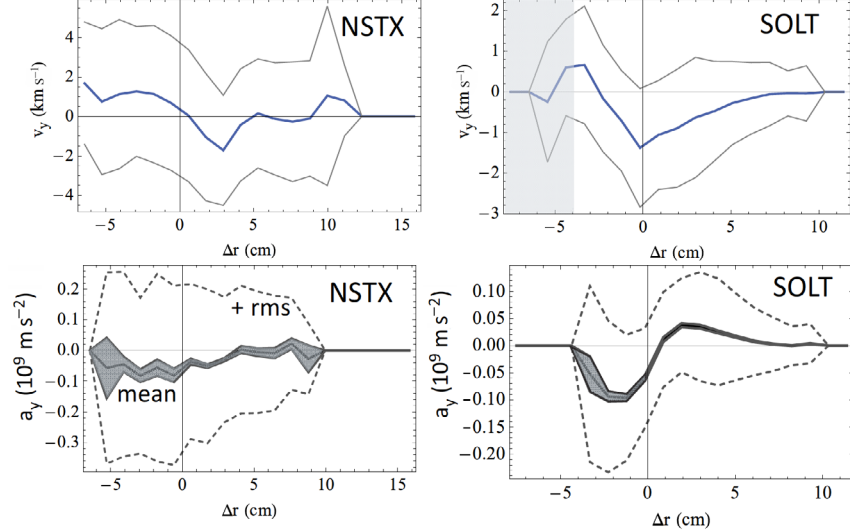


Figure 10. NSTX data (left) in comparison with SOLT simulation results (right). Top panels are radial profiles of the mean blob poloidal velocity v_y (thick blue line) and rms deviations (thin gray line). The shaded region in the upper-right SOLT figure may be influenced by the simulation boundary. Bottom panels show the mean blob acceleration a_y (gray shading indicates statistical uncertainty) and its rms deviations (dashed). Figure reproduced with permission from [88]. Copyright 2013 IAEA, Vienna.

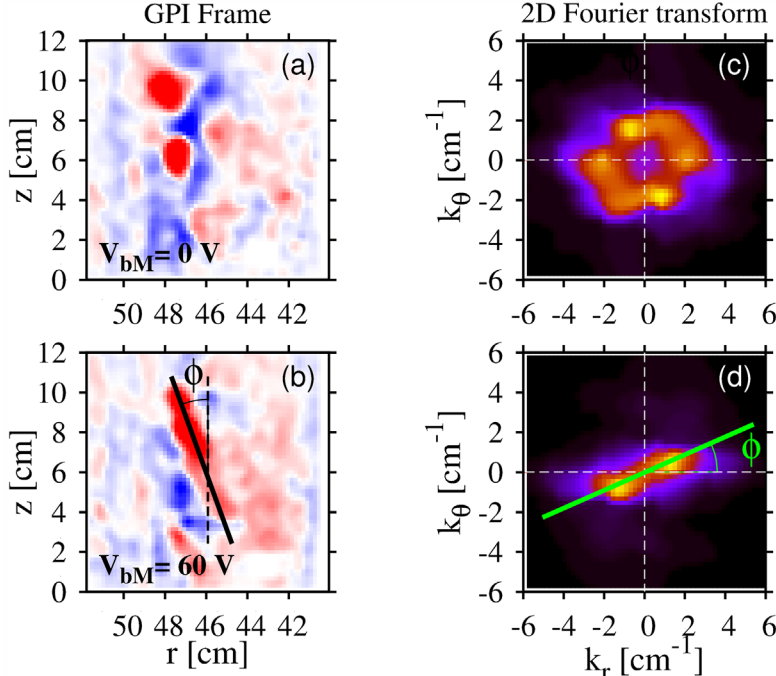


Figure 11. 2D mapping of density fluctuations via GPI in (a) unbiased and (b) biased plasmas (TEXTOR), showing the azimuthal elongation and tilt of eddy structures when electrode biasing (+60 V) is applied. The LCFS is at 47.5 cm; (c) radial/poloidal wavenumber spectrum without biasing; (d) radial/poloidal wavenumber spectrum with biasing. Figure reproduced with permission from [34]. Copyright 2013 by the American Physical Society.

demonstrate that a seed shear-flow layer can appear inside the LCFS well in advance of the L-H transition.

Clear evidence for the tilting of eddy structures has been obtained in linear and toroidal devices (e.g. [34], [90]) with electrostatic plasma biasing. Figure 11 shows the typical eddy topology and wavenumber spectrum with and without plasma biasing in the TEXTOR tokamak measured via GPI. Positive bias (~60 V) is applied via a biased electrode inserted to about 4 cm past the LCFS (located at 47.5 cm) [34]. A transition to H-mode with a marked increase of the line-averaged density is observed for higher bias voltage ~100–150 V.

Strong $E \times B$ flow shear exists with biasing both inside and outside the LCFS. Figure 11(a) shows a 2D plot of the fluctuating component of the GPI signal intensity (roughly proportional to plasma density) without biasing. Eddies are mostly circular, and the k_r, k_θ wavenumber spectrum (figure 11(c)) is quasi-symmetric. With positive bias, tilting and poloidal elongation of the eddy pattern is clearly observed (figure 11(b)), and the wavenumber spectrum (figure 11(d)) shows a characteristic asymmetry and reduction in poloidal wavenumber (corresponding to the increased poloidal extension of eddies).

It is well known that the L–H transition power threshold depends on the divertor geometry, in particular, on the direction of the ion grad- B drift with respect to the x-point/active divertor. The eddy topology away from the device midplane can be affected by the direction of the grad- B drift. It has been proposed that the difference in power threshold may be related to differences in the flux-surface-averaged Reynolds stress due to the combination of magnetic shear and $\mathbf{E} \times \mathbf{B}$ shear in both configurations [91, 92]. A direct test of this hypothesis may require turbulence imaging via off-midplane diagnostics. There is some experimental evidence that E_r shear is increased, and that the well structure of the $\mathbf{E} \times \mathbf{B}$ shear layer is more pronounced with a favorable drift direction in TORE SUPRA [92].

Early measurements of a finite Reynolds stress inside the LCFS include the work of Hidalgo *et al* in the TJ-II stellarator [93], where the Reynolds stress radial gradient was found to be comparable to the charge-exchange flow-damping rate. Evidence for poloidal flow drive across the transition to an ohmic H-mode regime was first reported in an early paper on the HT-6M tokamak [94]. The H-mode transition was induced via a turbulent heating (ohmic current) pulse. A comparison of the flow-acceleration term and the Reynolds-stress-gradient drive across the transition yielded a good match of both quantities during the turbulent heating/initial flow acceleration phase where poloidal flow damping could be neglected. More recently, several other experiments have provided estimates of the magnitude of the Reynolds stress gradient across the L–H transition. These investigations use specialized array probes simultaneously measuring radial and poloidal floating-potential fluctuations to extract the fluctuating $\mathbf{E} \times \mathbf{B}$ velocity components, and the mean $\mathbf{E} \times \mathbf{B}$ flow velocity. Probe data taken during L-mode-LCO transitions in DIII-D have shown that the Reynolds stress well inside the LCFS, within the L-mode electric-field well, increases periodically at the exact time when $\mathbf{E} \times \mathbf{B}$ flow acceleration in the negative (electron diamagnetic) direction is observed [36]. Similarly, probe data and velocimetry based on GPI data in the EAST tokamak [30, 35, 53, 54] and in TEXTOR [34] have provided estimates of the Reynolds stress gradient during I-phase and across fast L–H transitions. Using estimated flow-damping rates, it has been concluded in these studies that the Reynolds stress gradient is sufficiently large to explain the observed change/acceleration in $\mathbf{E} \times \mathbf{B}$ velocity across the L–H transition within experimental accuracy.

The turbulence–flow energy transfer preceding the L–H transition has been quantitatively determined in a number of experiments [35, 36, 38, 39, 52, 53]. A simple 1D model has been successfully used to describe this transfer. The governing equations describing energy conservation for the turbulent energy density (with timescales characteristic of drift-wave turbulence) and low-frequency flow energy are equivalent to a simplified form of the so-called K - ε model equations in fluid dynamics [95, 96]:

$$\frac{\partial \widetilde{K}}{\partial t} = \gamma_{\text{eff}} \widetilde{K} - P - \frac{\partial \widetilde{T}}{\partial r} \quad (2)$$

$$\frac{\partial \overline{K}}{\partial t} = P - \frac{\partial \overline{T}}{\partial r} - \nu_{\text{LF}} \overline{K}. \quad (3)$$

Here, we introduce the following abbreviations:

$$\begin{aligned} \widetilde{K} &= \frac{1}{2} \langle \tilde{v}_\perp^2 \rangle, \quad \widetilde{T} = \frac{1}{2} \langle \tilde{v}_r \tilde{v}_\theta^2 \rangle, \quad \overline{K} = \frac{1}{2} \langle v_\theta^2 \rangle, \quad \overline{T} = \langle \tilde{v}_r \tilde{v}_\theta \rangle \langle v_\theta \rangle \\ \text{and } P &= \langle \tilde{v}_r \tilde{v}_\theta \rangle \frac{\partial v_\theta}{\partial r}, \end{aligned}$$

where v_\perp designates the perpendicular turbulent flow velocity, v_θ is the (low-frequency) driven flow, \widetilde{K} and \overline{K} are the turbulence and driven-flow kinetic energy, and \widetilde{T} and \overline{T} signify the radial flux of turbulence intensity (turbulence spreading) and the radial spreading of the low-frequency flow. $P - \partial \overline{T} / \partial r$ signifies the total Reynolds work; $P + \partial \widetilde{T} / \partial r$ is the total energy loss from the turbulence spectrum including radial turbulence spreading. In addition, γ_{eff} is the effective (L-mode) turbulence linear growth rate, and ν_{LF} is the (low-frequency) flow-damping rate. Equation (2) describes the kinetic energy evolution of the turbulence with the Reynolds work as the sink term, while equation (3) describes the (low-frequency) flow evolution driven by the Reynolds work as the source term, with a collisional-dissipation term. The exact form of the flow-damping term depends on the collisionality regime, as discussed above. If the radial ‘spreading terms’ \widetilde{T} and \overline{T} are neglected, the model reduces to 0D. A separation of timescales between the ‘fast’ turbulent quantities and the low-frequency or ‘mean’ ion flow is assumed here. Similar to the ion momentum equation (1) discussed previously, the poloidal flow inertia can be incorporated as a screening term in equation (3). Turbulence suppression via energy transfer to driven flows requires that the total turbulence drive $\gamma_{\text{eff}} \widetilde{K}$ is balanced by the Reynolds work, a condition that can be expressed as

$$R_T = \frac{P + \partial \overline{T} / \partial r}{\gamma_{\text{eff}} \widetilde{K}} > 1. \quad (4)$$

Figure 12 shows measurements from an L–H transition in the C-Mod tokamak, where GPI [38] has been used to extract the density-fluctuation level and the turbulence advection velocity [97, 98]. These measurements were carried out at substantially higher magnetic field ($B_\phi = 5.4$ T) and L-mode separatrix (LCFS) plasma density ($n_{\text{sep}} \sim 1 \times 10^{20} \text{ m}^{-3}$) compared to the ASDEX-U and DIII-D data discussed below, at similar q_{95} . Figure 12(a) shows the evolution of the energy-transfer coefficient R_T (equation (4)) during the L–H transition. R_T is substantially larger than one at the time when the turbulence kinetic energy decreases (figure 12(b)) and when the $\mathbf{E} \times \mathbf{B}$ velocity increases (figure 12(c)). The time evolution clearly shows that the extracted $\mathbf{E} \times \mathbf{B}$ flow velocity increases concomitantly with the decrease in turbulence level, and that both changes occur before a significant increase in the line-integrated plasma density (figure 12(d)). The electron pressure gradient (figure 12(e)), similar to the density, increases substantially only after the turbulence–flow coupling has increased the $\mathbf{E} \times \mathbf{B}$ velocity. The electron pressure gradient is used here as a proxy of the ion pressure gradient due to the strong coupling of the electron and ion fluid and the resulting equilibration of temperatures. The data indicate clearly that the ion energy-transfer coefficient R_T and the $\mathbf{E} \times \mathbf{B}$ flow change prior to the local increase of the density/pressure

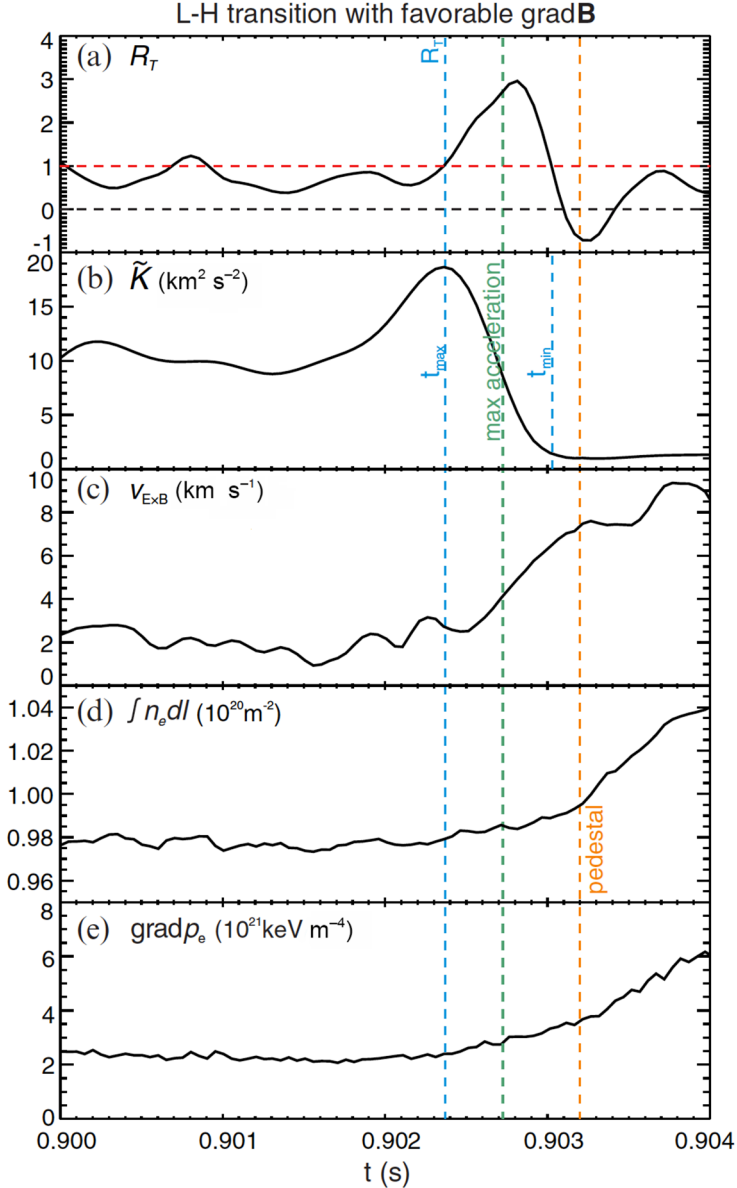


Figure 12. Evolution of key parameters in the L–H transition in Alcator C-Mod: (a) nonlinear kinetic-energy transfer rate R_T (energy transfer to low-frequency flow normalized by turbulence energy growth); (b) turbulent kinetic energy; (c) $E \times B$ velocity evaluated from the GPI advection velocity; (d) line-integrated plasma density; dashed lines indicate the time when the energy-transfer coefficient R_T reaches unity, the time of maximum flow acceleration, and the end of the flow production burst. The pedestal pressure gradient is plotted in (e), calculated assuming $T_e \sim T_i$. Figure reproduced with permission from [97]. Copyright 2015 IAEA, Vienna.

gradient. Further analysis has shown that the ion bulk flow velocity increment is dominant preceding the transition.

An analysis of the energy transfer has also been carried out in DIII-D. Beam emission spectroscopy data in the DIII-D tokamak also show clearly that the energy-transfer rate exceeds the effective turbulence growth rate prior to the L–H transition [39, 82]. Figure 13 shows the time evolution of the energy-transfer rate across a ‘fast’ L–H transition for three radial positions. The data nearest to the LCFS ($\rho = 0.98$, where $\rho = r/R$ is the normalized minor radius) show a transient peak just prior to the L–H transition, which occurs at $t = 1558.1$ ms (identified experimentally by the turbulence suppression time), while no significant change in the transfer rate is observed for smaller minor radii. The maximum energy-transfer rate at $\rho = 0.98$ exceeds both the effective growth rate

γ_{eff} and the turbulence decorrelation rate. The condition for turbulence suppression stated in equation (4) is satisfied in DIII-D when LCOs start, as discussed in [36], and in single-step L–H transitions in DIII-D and other experiments [35, 38, 39]. The numerical equivalence between the suppression condition derived in the K - ε model, and the shear-suppression criterion has been discussed in [64]. Here, it is shown that, within numerical factors of the order of one, the turbulence ‘quench rule’ is equivalent to the K - ε model turbulence-suppression criterion (equation (4), neglecting radial turbulence spreading).

It should be noted that turbulence-driven mean flows and zonal flows can often not be clearly distinguished in the experiments as they have, in practice, very similar or identical experimental signatures. Theoretically, ZFs are often thought of as radial mesoscale structures with a typical radial scale

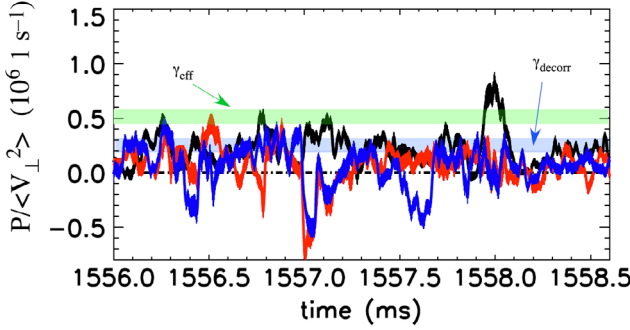


Figure 13. Time evolution of the flow production rate, approaching the L–H transition, for three different radii in DIII-D: black is at $\rho \sim 0.98$, light gray (red) is at $\rho \sim 0.96$, and dark gray (blue) is at $\rho \sim 0.93$. The production rate increases at the outer radius just before the L–H transition at 1558.1 ms. The line thickness is the systematic error bar. The estimated range of the turbulence’s effective growth rate and decorrelation rate is shown for comparison. Figure reproduced with permission from [39]. Copyright 2014 by the American Physical Society.

length between the ion gyroradius and the macroscopic pressure-gradient scale length. In practice, however, it may be difficult to distinguish the mesoscale from the pressure-gradient scale in the plasma edge as they may only differ by a factor of 2–3. Additionally, in the core plasma, zonal flows may form and decay on the timescale of the turbulence correlation time. This would then set a timescale that is shorter than the characteristic timescale of mean flows. However, in the plasma edge, particularly in the presence of strong spectral condensation, these timescales may not be well separated.

6. Recent L–H transition modeling results

6.1. Heuristic models

Reduced heuristic models of turbulence–flow interaction at the L–H transition date back to the early 1990s [19, 24–26] and have evolved from simple 0D Lotka–Volterra predator–prey models to 1D simulations including particle/heat radial transport and the radial ion-momentum balance. A transition from an intermediate oscillatory limit-cycle state to a state with sustained turbulence suppression was first described by Kim and Diamond [26]. In addition to predator–prey dynamics and the effect of ZF shear, this model includes pressure-profile evolution and the effect of equilibrium (diamagnetic) flow shear on turbulence evolution. Recently, substantially advanced 1D models have been developed which include neoclassical and anomalous radial heat/particle transport with more realistic radial source distributions, as well as poloidal ion (mean) flow evolution and neoclassical ion flow damping [58–60, 65]. The model described in [58, 59] considers turbulence driven by the ITG, based on a simple critical-gradient model. Figure 14 shows results from a 1D calculation of the self-consistent evolution of the $\mathbf{E} \times \mathbf{B}$ shearing rate associated with diamagnetic flow $\omega_{E \times B, dia} = L_n^{-1} L_p^{-1} c_s \rho_i$, where L_n and L_p are the density and ion pressure-gradient scale lengths (figure 14(a)), and the normalized energy-transfer rate from the turbulence into the zonal flow, $\alpha_0 E_0 / (\gamma_L - \Delta\omega I)$ (figure 14(b)). The ratio of

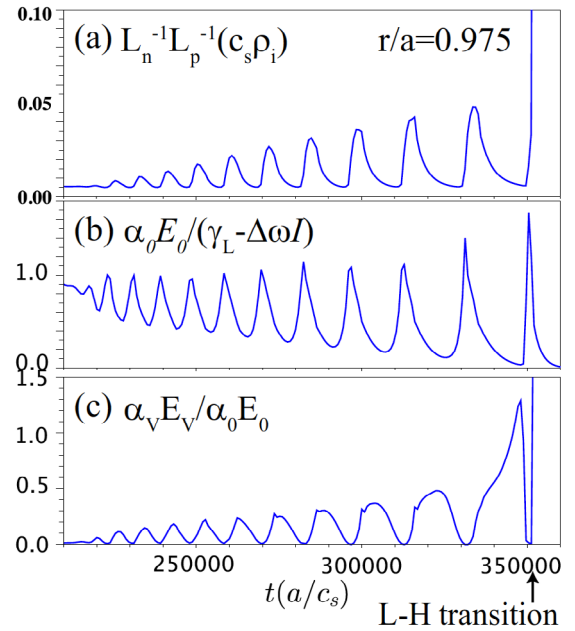


Figure 14. Time evolution of (a) $\mathbf{E} \times \mathbf{B}$ shearing rate due to diamagnetic flow, (b) the turbulence energy transferred to the ZF, normalized by the net energy input into the turbulence, and (c) the ratio of mean flow (MF) shear to ZF shear, from the onset of I-phase at $t = 2.1 \times 10^5$ (a/c_s) to the L–H transition indicated at $t = 3.5 \times 10^5$ (a/c_s), in the edge region at $r/a = 0.975$. Throughout the I-phase, the $\mathbf{E} \times \mathbf{B}$ shearing rate due to diamagnetic flow oscillates with increasing amplitude. At the last cycle at $t = 3.5 \times 10^5$ (a/c_s), ZF shearing is strongly enhanced, and sufficient to quench the turbulence. Then, the mean shear is sufficient to lock in the H-mode transition. Figure taken from [58], with the permission of AIP Publishing.

the mean shear flow to the ZF shear-flow energy density is shown in figure 14(c). Here, $E_0 = V_{ZF}^{1/2}$ indicates the energy density of the zonal shear flow, γ_L , $\Delta\omega$, and I are the linear growth rate, frequency broadening induced by nonlinear turbulence saturation, and turbulence intensity, and α_0 is the ZF shear coupling coefficient [58] related to the Reynolds work via $P = \langle \tilde{v}_r \tilde{v}_\theta \rangle \partial v_\theta / \partial r = \alpha_0 E_0 I$ (radial turbulence spreading is neglected here). Figure 14(a) indicates that the pressure-gradient modulation is small initially during LCO (in agreement with experimental results [32], but becomes dominant close to the LCO-H-mode transition. Figure 14(b) shows clearly that the peak energy input into oscillating shear flows approximately matches the turbulent energy growth periodically during LCO ($\alpha_0 E_0 / (\gamma_L - \Delta\omega I) \sim 1$), and substantially exceeds turbulent energy growth just preceding the LCO-H-mode transition ($\alpha_0 E_0 / (\gamma_L - \Delta\omega I) > 1$). Figure 14(c) shows the ratio of the mean shear-flow energy density to the ZF shear-flow energy density $\alpha_v E_v / \alpha_0 E_0$, where α_v is the mean flow-shear coupling coefficient [58] and E_v is the mean shear-flow energy density. This ratio exceeds unity just preceding the LCO-H-mode transition, indicating that dominant mean flow shear is the critical condition to lock in the H-mode.

An extended version of this model, with separate equations describing radial energy balance for electrons and ions, has been employed to calculate the effects of preferential electron and ion heating on the L–H transition power threshold

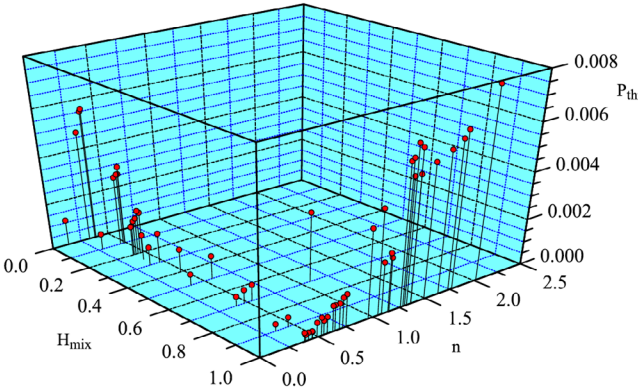


Figure 15. 3D scatter-plot of transition power threshold P_{thr} as extracted from modeling, versus ion/electron heating mix and density, H_{mix} and n . The choice of n , H_{mix} points in the sample is dictated by the experimental trend of electron-biased heating at lower densities and ion-biased heating at higher densities. However, an extended subsample at $H_{\text{mix}} = 1$ (pure ion heating) is also included in the plot. Figure taken from [60], with the permission of AIP Publishing.

[60]. In addition to an ITG linear growth rate based on a simple critical-gradient model, TEM (trapped electron mode) turbulence driven by density and electron-temperature gradients was heuristically accounted for, neglecting a possible critical-gradient effect. This work was motivated by the non-monotonic dependence of the L–H transition power threshold on plasma density, and by recent experimental results from the AUG tokamak which suggest that the increasing power threshold at low density is related to increased electron thermal loss [99–101]. In these experiments, employing selective electron heating, ion and electron thermal transport are collisionally decoupled at low density. It has been observed that the power threshold increased with electron heating and separatrix electron temperature. However, the ion diamagnetic L-mode flow and flow shear (which are related to the local ion temperature and pressure gradient and determine mean flow shearing inside the LCFS in L-mode) decreased with decreasing density. These results indicate that the increase of the L–H power threshold at low density may be the result of additional electron energy loss. Figure 15 shows 1D modeling results obtained by scanning the L-mode density and the electron/ion heating mix. Malkov and Diamond observed that the calculated power threshold attains a minimum at low density and maximum ion heating [60], but increases at low density and increased electron heating. Thus, the calculated power threshold exhibits a similar trend to the experimentally observed increase of the power threshold at low density with preferential electron heating [100, 101].

LCO and one-step L–H transitions were also observed in modeling results considering only momentum transport and the interaction of turbulent fluctuations with the mean shear flow [62]. In these 0D and 1D calculations, the parallel and toroidal momentum equations, including Reynolds stress terms proportional to the turbulence intensity, are solved. The turbulence growth rate is obtained from linear gyrokinetic calculations based on an actual DIII-D L-mode equilibrium, and a spectral-shift model [63] is employed to account for the effect of $\mathbf{E} \times \mathbf{B}$ shear on the turbulence. For a 1D extension, the diamagnetic velocity is ramped in time, implementing a specified radial

pressure profile based on experimental data. LCO or (one-step) L–H transitions are driven in this model by the competition between the growth of the $\mathbf{E} \times \mathbf{B}$ flow drive and the growth of the parallel velocity. Sheared $\mathbf{E} \times \mathbf{B}$ flow leads to turbulence reduction; however, the radial turbulence intensity modulation leads to sheared parallel flow and deceleration of the $\mathbf{E} \times \mathbf{B}$ flow, resulting in $\mathbf{E} \times \mathbf{B}$ and parallel-flow oscillations. The parallel flow shear can also be a destabilizing factor. The 0D model can produce LCOs for experimental parameters where L-mode-LCO transitions were observed in DIII-D, approximately matching the experimentally observed LCO frequency and $\mathbf{E} \times \mathbf{B}$ velocity modulation [32]. Calculations were carried out for collisionalities in the Pfirsch–Schlüter regime. The model predicts a characteristic increase in the parallel velocity once the $\mathbf{E} \times \mathbf{B}$ velocity has increased sufficiently within an LCO cycle. Further experiments will address parallel-flow acceleration and the competition between $\mathbf{E} \times \mathbf{B}$ flow and parallel flow to test these model predictions. The model has been expanded recently, including particle and energy-transport equations in 0D and 1D, and 1D oscillating solutions with LCO frequencies in the range of experimental data have been obtained for specific boundary conditions [64] (fixed toroidal $\mathbf{E} \times \mathbf{B}$ velocity and vanishing flux-surface-averaged parallel velocity at the LCFS).

6.2. L–H transitions in fluid models

LCO and L–H transition simulations have also been carried out using fluid models based on the Braginskii equations (or reduced equation sets based on the Braginskii equations) [66–73]. One can expect that the dominant L-mode turbulence modes at the edge depend on collisionality. RBM may be important or dominant at high collisionality in the Pfirsch–Schlüter regime whereas TEM/ITG-type turbulence may be dominant at low collisionality where trapped particle effects can be expected.

The fluid models discussed here are most appropriate in the high-collisionality (Pfirsch–Schlüter) regime, and assume $k_{\perp}\rho_s \ll 1$ for the dominant modes. Earlier work, using 3D toroidal flux-tube geometry and the complete set of Braginskii equations, already demonstrated a transition driven by a transient turbulence-generated poloidal flow, and a subsequent increase of the ion pressure gradient/diamagnetic flow reflected in the formation of a pronounced electric-field well maintaining turbulence suppression [66]. In the first example of more recent work described here, a four-equation model has been applied to simulate low-frequency interchange-driven turbulence, including dissipation and finite ion temperature [70]. The continuity and vorticity equations are solved along with ion and electron energy conservation equations for local slab geometry, retaining the magnetic-field curvature. The simulations include ‘core’ and ‘SOL’ regions and account for the transition between both domains. Transport parallel to the magnetic field in the SOL is taken into account via characteristic loss rates for parallel particle flow and ion/electron heat flow. The plasma parameters used in these simulations are characteristic of the Pfirsch–Schlüter (high collisionality) regime, based on typical separatrix parameters in (low-power or ohmic) EAST and ASDEX-U discharges. Geometry parameters are $R = 2.0$ m, $a = 0.5$ m, $B = 2.0$ T, and $q_{95} = 4.5$. Separatrix parameters are

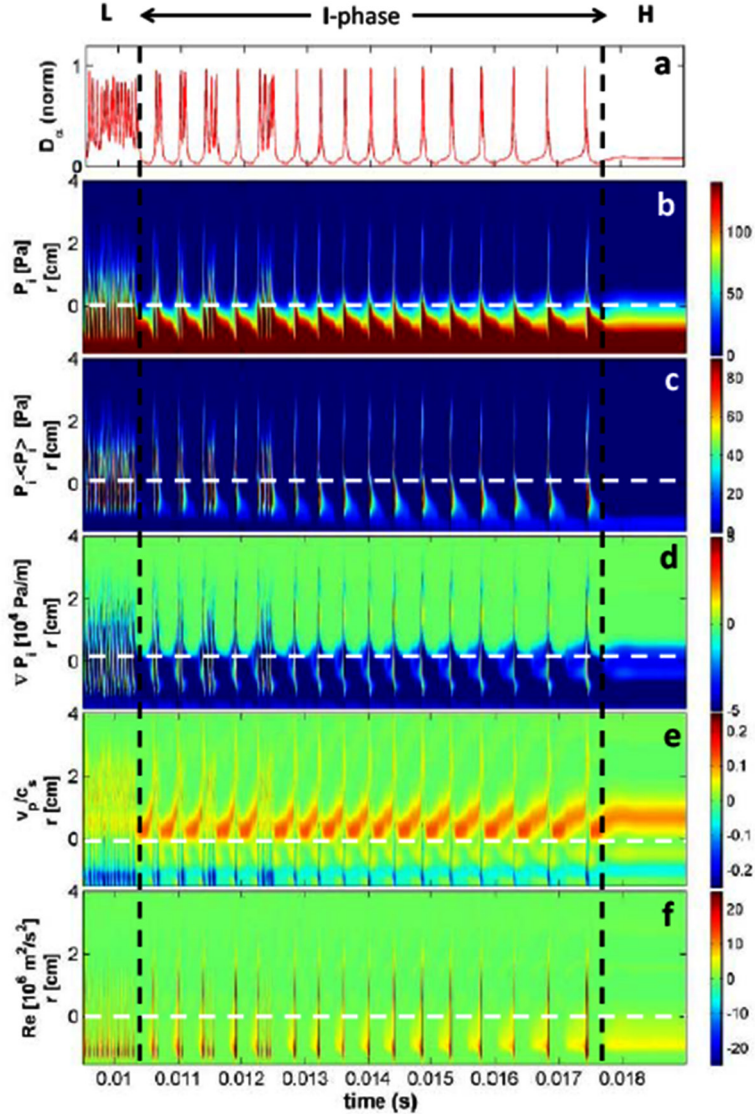


Figure 16. 1D fluid simulation of the L–I–H transition. (a) Integrated parallel particle loss term as a proxy for divertor D_α signal; (b) ion pressure-profile evolution; (c) ion pressure-profile fluctuations; (d) radial profile of ion pressure gradient; (e) poloidal $\mathbf{E} \times \mathbf{B}$ flow profile; (f) Reynolds stress derived from turbulent $\mathbf{E} \times \mathbf{B}$ velocities. The horizontal dashed lines mark the LCFS ($r = 0$). The frames (b)–(f) do not contain the inner region ($r < -1.5$ cm), where equilibrium profiles are forced. Figure reproduced with permission from [70]. Copyright 2015 IOP Publishing.

$kT_{e\text{sep}} = 20\text{ eV}$, $kT_{i\text{sep}} = 20\text{ eV}$, and $n_{\text{sep}} = 1.5 \times 10^{19}\text{ m}^{-3}$. The model predicts both fast L–H transitions (via a fast ramp of the ion temperature/radial ion heat flux), and LCO transitions, as shown in figure 16. Here, panel (a) shows the integrated parallel SOL particle-loss term used as a proxy for the D_α recycling light, showing intermittent/periodic reduction during the LCO phase, and sustained reduction after the LCO–H-mode transition. The ion pressure profile, shown in a contour plot in figure 16(b), steepens considerably during the ‘quiet’ LCO periods and in H-mode, and the pressure fluctuations (figure 16(c)) decrease concomitantly with a periodic increase in the radial ion pressure gradient (figure 16(d)) and the $\mathbf{E} \times \mathbf{B}$ flow shear across the LCFS (figure 16(e)). During the ‘quiet’ periods, the maximum of the $\mathbf{E} \times \mathbf{B}$ velocity moves radially outwards from the LCFS, reducing the local shear at the LCFS. This results in a burst of turbulence extending several cm into the SOL, increasing local radial transport and reducing

the ion pressure gradient. The Reynolds stress (figure 16(f)) increases strongly during these turbulence bursts and could be instrumental in re-establishing the increased $\mathbf{E} \times \mathbf{B}$ shear flow. There is a finite intermittent Reynolds stress present inside the LCFS in the ‘L-mode’ phase preceding the start of LCO. The Reynolds stress (gradient) does not appear to increase prior to LCO, but increases substantially during the LCO turbulence bursts in the simulation result, in agreement with several of the experimental findings [36, 53].

An earlier electromagnetic 3D fluid simulation has been carried out for L-mode parameters, using a realistic DIII-D magnetic equilibrium (single-null x-point configuration) [72] including the SOL and outer core regions. The seven-field equation set based on a reduced Braginskii model with drift-wave ordering includes continuity, vorticity, ion/electron energy transport, and parallel ion/electron momentum equations. L-mode turbulence is found to be dominated by

resistive x-point modes and subdominant high-n ballooning modes. The calculations demonstrate a transition with substantial reduction in high-n modes via Reynolds-stress-driven poloidal flow/ $E \times B$ flow. The (poloidally asymmetric) radial current pattern associated with the Reynolds stress gradient has been extracted. Interestingly, no substantial difference in the driven poloidal flow/ $E \times B$ flow was found for favorable/unfavorable grad- B drift directions.

Other more recent simulations based on reduced MHD equations appropriate for simulating RBM turbulence have been also reported [67–69]. In a flux-driven 3D simulation, Chôné *et al* obtained a plasma edge barrier where the $E \times B$ flow is driven by the radial gradient in neoclassical friction [67, 69]. Neoclassical friction was found to be mostly a driver for the shear flow before edge barrier formation, whereas Reynolds stress acted intermittently as both a source and a sink. After the transition the Reynolds stress was found to be mainly a sink (transferring flow energy back to the turbulence), whereas neoclassical friction remained a source of the $E \times B$ shear flow. Intermittent LCOs were also found, where the $E \times B$ flow collapses and fluctuations peak.

A reduced fluid equation set (vorticity and pressure advection equations) has been used to simulate electrostatic resistive ballooning turbulence in a more recent simulation by Park *et al* [68] within the framework of the BOUT++ code, and has demonstrated the temporal sequence of the L–H transition. The simulation is appropriate for the collisional regime, with the normalized ion collisionality reaching $\nu_i^* \sim 10 - 100$ near the separatrix. A clear LCO phase is found before the L–H transition, and the pressure gradient increases after the $E \times B$ velocity during the LCO-H-mode transition. The energy-transfer coefficient (equation (4)) increases beyond unity prior to the increase of the ion pressure gradient at the transition. The conventional turbulence quench criterion, $\omega_{E \times B} > \gamma_L$, however, is only fulfilled after the $E \times B$ shearing rate increases further due to positive feedback with the increasing pressure gradient. The transition has been confirmed as a first-order phase transition from the dependence of the pressure gradient on input power in the simulation: beyond a critical power input the pressure gradient increases more rapidly with increasing heating power.

7. Discussion and conclusions

Turbulence–flow interaction across the L–H and L-mode-LCO (I-phase) transition has been investigated in detail in a large number of devices over the last few years, taking advantage of substantial improvements in the spatial and temporal resolution of diagnostics. Understanding of the microscopic physical picture of shear-flow generation has substantially progressed. L-mode-LCO/I-phase transitions and one-step L–H transitions have enabled the separation of the initial phase of flow generation (the trigger phase) from the more gradual pressure-profile evolution and an increase in $E \times B$ shear flows arising due to the diamagnetic drift in several experiments [29, 32, 35, 36, 38, 39, 50–52, 97, 98]. Progress has also been made in quantifying the nonlinear energy transfer from turbulence to flows, using a simplified K - ε transfer model based on

hydrodynamics [34, 36, 38, 39, 97, 98]. The transfer process has been analyzed both in so-called ‘fast’ L–H transitions and in transitions characterized by intermediate LCO (or I-phase). Energy-transfer coefficients well in excess of one have been confirmed immediately preceding the transition, as required for rapid turbulence quench. We wish to point out, however, that several experiments do not reveal a clear separation between flow generation and pressure-profile modification/increase in diamagnetic flow and flow shear across the L–H transition, pertaining to fast L–H transitions [101–103] but also L-mode-LCO transitions [57, 104]. It is unknown at this time, which characteristics lead to these observed differences. The present expansion/duplication of diagnostics with high temporal/spatial resolution on several devices may allow these issues to be addressed.

Turbulence–flow interaction is also important in the context of H–L back-transitions. Preliminary data on the back-transition sequence have been obtained [50, 105], and hysteresis has been observed between the L–H transition threshold power and the power level where a back-transition is initiated. In regimes where LCOs are present, the back-transition is typically initiated by transients resembling type I or type III ELMs, although well below peeling-balloonning stability limits [106, 107]. The energy release and the evolution of sheared flow during the back-transition have been investigated for a specific scenario [106, 107]. Once the pedestal pressure gradient has been substantially reduced, LCOs with increasing frequency are often observed before an LCO-L-mode transition occurs with increasing turbulence. The H–L transition hence reverses the time evolution of the L–H forward transition. The H–L back-transition is important in the context of a safe ramp-down of the stored energy (‘safe landing’) of burning plasma discharges without undue stresses on the poloidal coil systems, which is challenging.

While significant progress has been made addressing microscopic turbulence–flow interaction, a physics-based model of the power-threshold scaling is desired. It is now crucial to link microscopic transition physics to the power-threshold scaling in a systematic way. Initial work towards this goal is reported in [4–8, 51, 60, 62, 65, 82, 99–101]. In order to make this connection, several aspects need to be considered. L-mode turbulence may exhibit significant differences in growth rate, nonlinear saturation mechanism, and saturated wavenumber spectrum depending on edge collisionality. Typically the separatrix region transitions from the plateau to the Pfirsch–Schlüter regime at intermediate density ($n_{sep} \sim 1-2 \times 10^{19} \text{ m}^{-3}$ for typical edge ion temperatures). Depending on the dominant turbulence regime, the eddy topology may be more or less susceptible to pre-existing L-mode-edge shear flow (driven by the L-mode pressure gradient or L-mode neoclassical ion flow). Secondly, the L-mode flow shear enters directly into the Reynolds work (equation (3)) and the energy-transfer coefficient defined in equation (4). Differences in L-mode shear, e.g. related to collisionality, plasma geometry/shape, main ion species, or atomic physics may, therefore, influence the energy transfer to turbulence-driven flows. Perhaps most importantly, however, L-mode shear depends on the L-mode-edge pressure gradient determined by outer core transport and the SOL boundary conditions. L-mode outer-core turbulent transport

and the relevant critical temperature/density gradients determine the ion pressure gradient inside and across the separatrix. In AUG experiments, ion and electron thermal radial transport have been decoupled in low-density ECH plasmas, and the upturn in the L–H power threshold at low density has been attributed to the additional power loss in the electron channel at high-separatrix electron temperature [99–101]. After accounting for the additional electron-channel power loss, the L–H power threshold was found to increase in proportion to the ion heat flux. The majority of investigations of turbulence–flow interaction have been made at intermediate density/magnetic field, near the respective power threshold minimum in the different devices. Detailed measurements at very low and high density will be necessary to discriminate different physical processes or assess the effects of potential changes in poloidal flow damping/zonal flow damping at different collisionality. It is well known that the L–H transition power threshold increases substantially for reversed grad-*B* drift direction. In view of recent theoretical predictions [91, 92] detailed experiments in plasmas with reversed grad-*B* drift may provide important insights into turbulence/eddy topology prior to the L–H transition. Furthermore the influence of geometry effects (x-point height, parallel connection length, and divertor geometry) is important, but has not been investigated sufficiently with respect to their influence on turbulence properties and flows.

It is important to note that L–H transitions can be triggered in ways other than via turbulence–flow interactions if the edge pressure gradient is directly manipulated via a heat pulse from the core, or via the addition of a strong local particle source [108]. Examples include L–H transitions triggered by sawteeth or core MHD activity releasing a heat pulse (e.g. [56]). Experiments with small pellet injection in DIII-D [109], or with supersonic molecular beam injection (SMBI) in KSTAR [108] have triggered L–H transitions via the steepening of the edge density (pressure) gradient (due to the localized pellet-ionization source). The sheared $\mathbf{E} \times \mathbf{B}$ flow balancing the diamagnetic flow increased in these cases to a value sufficient to sustain the H-mode transport barrier. In DIII-D, the L–H power threshold was reduced by more than 20% with pellet injection; reductions from 30–50% have been observed with SMBI, although maintaining the H-mode state required repeated SMBI injections. Heuristic models describing stimulated/induced L–H transitions have been developed [110, 111].

Modeling and simulations of L–H transitions have substantially expanded over the last few years, and heuristic models as well as fluid models have been widely applied. Initial results based on global 2D/3D electromagnetic fluid codes are reported in [71, 72]. Reduced models are very valuable for exploring certain aspects of transition physics, and for performing simple parameter scans. Reduced fluid models have been focused on modeling ideal or resistive interchange turbulence [70, 73], or resistive ballooning turbulence [66–69]. In the latter case, the vorticity equation has been solved along with the continuity and ion momentum equations, including parallel resistivity. Eventually, however, first-principles simulations will require the full set of Braginskii equations in 3D to take into account

the full fluctuation/flow dynamics parallel to the magnetic field, in realistic toroidal geometry. An additional complication is the treatment of the transition between the closed and open field-line region requiring correct implementation of sheath boundary conditions for the SOL. Several modeling results show a poloidal flow increase concomitantly with an ion pressure-gradient increase at the transition [64, 65]. Other simulations results do not show a clearly separated trigger signature in advance of the increase in the pressure gradient/diamagnetic flow [70]. Simulations closely matched to experimental parameters across an extended density/collisionality range may provide additional insight into the cause for these differences, and potential variations in the trigger physics or its parameter dependence. Gyrokinetic modeling of the L–H transition still faces substantial obstacles and would require global nonlinear simulations with large parameter variations across the simulation domain, as well as different parallel boundary conditions in the core and SOL regions. However, gyrokinetic simulations of the L-mode plasma edge inside the LCFS have become feasible and should provide substantial new insight regarding the differences in L-mode turbulence characteristics and transport fluxes between the low-density and high-density branches of the power-threshold scaling, and their isotopic dependence. In this respect the recent progress made in the modeling of the L-mode outer core is encouraging (addressing the so-called ‘transport shortfall’ observed sometimes in gyrokinetic L-mode core simulations). This work has important implications for understanding L-mode transport and the structure/properties of L-mode turbulence preceding the L–H transition.

Acknowledgments

The author would like to acknowledge valuable, stimulating discussions with G.R. McKee, Z. Yan, P.H. Diamond, P. Gohil, K. Itoh, M. Malkov, G. Tynan, G. Staebler, T.L. Rhodes, K.H. Burrell, B. Grierson, C. Chrystal, I. Cziegler, G.S. Xu, G. Conway, S. Zweber, and J. Myra.

This work was supported by the US Department of Energy under DE-FG02-08ER54984 and DE-FC02-04ER54698.

References

- [1] Wagner F. *et al* 1982 *Phys. Rev. Lett.* **49** 1408
- [2] Wagner F. 2007 *Plasma Phys. Control. Fusion* **49** B1
- [3] Martin Y.R. and Takizuka T. 2008 *J. Phys.: Conf. Ser.* **123** 012033
- [4] Gohil P. *et al* 2011 *Nucl. Fusion* **51** 103020
- [5] McKee G.R. *et al* 2009 *Nucl. Fusion* **49** 115016
- [6] Ryter F. *et al* 2009 *Nucl. Fusion* **49** 062003
- [7] Gohil P. *et al* 2011 *Nucl. Fusion* **50** 064011
- [8] Ryter F. *et al* 2013 *Nucl. Fusion* **53** 113003
- [9] Biglari H., Diamond P.H. and Terry P.W. 1990 *Phys. Fluids B* **2** 1
- [10] Burrell K.H. 1997 *Phys. Plasmas* **4** 1499–518
- [11] Burrell K.H. 1999 *Phys. Plasmas* **6** 4418
- [12] Ritz C.P., Bengtson R.D., Levinson S.J. and Powers E.J. 1984 *Phys. Fluids* **27** 2956–9
- [13] Rettig C.L. *et al* 1993 *Nucl. Fusion* **33** 643–7
- [14] Tynan G.R. *et al* 1994 *Phys. Plasmas* **1** 3301

